3D characterization and plasmon mapping of gold nanorods welded by femtosecond laser irradiation

3D Characterization and Plasmon Mapping of Gold Nanorods Welded by Femtosecond Laser Irradiation

Thaís Milagres de Oliveira[1,2,‡], Wiebke Albrecht[1,2,‡,*], Guillermo González-Rubio[3,5], Thomas Altantzis[1,2], Ivan Pedro Lobato Hoyos[1,2], Armand Béché[1,2], Sandra Van Aert[1,2], Andrés Guerrero-Martínez[5], Luis M. Liz-Marzán[3,4,6], Sara Bals[1,2,*]

[1] EMAT, University of Antwerp, Groenenborgerlaan 171, B-2020 Antwerp, Belgium.

[2] NANOlab Center of Excellence, University of Antwerp, Groenenborgerlaan 171, B-2020 Antwerp, Belgium.

[3] CIC biomaGUNE, Basque Research and Technology Alliance (BRTA), Paseo de Miramón 182, 20014 Donostia–San Sebastián, Spain.

[4] CIBER de Bioingeniería, Biomateriales y Nanomedicina (CIBER-BBN), Paseo de Miramón 182, 20014 Donostia–San Sebastián, Spain.

[5] Departamento de Química Física, Universidad Complutense de Madrid, Avenida Complutense s/n, 28040 Madrid, Spain.

[6] Ikerbasque (Basque Foundation for Science), 48013 Bilbao, Spain.

ABSTRACT Ultrafast laser irradiation can induce morphological and structural changes in plasmonic nanoparticles. Gold nanorods in particular can be welded together upon irradiation with femtosecond laser pulses, leading to dimers and trimers through the formation of necks between individual nanorods. We used electron tomography to determine the 3D (atomic) structure at such necks for representative welding geometries and to characterize the induced defects. The spatial distribution of localized surface plasmon modes for different welding configurations was assessed by electron energy-loss spectroscopy. Additionally, we were able to directly compare the plasmon linewidth of single-crystalline Au NRs and welded Au NRs with single defects at the same resonance energy, thus making a direct link between the structural and plasmonic properties. In this manner, we show that the occurrence of (single) defects results in significant plasmon broadening.

KEYWORDS: welded gold nanorods; femtosecond laser excitation; plasmonics; electron tomography; electron energy loss spectroscopy; plasmon linewidth; structural defects.

The interaction of gold nanoparticles (Au NPs) with light is largely determined by coherent oscillations of conduction electrons at resonant frequencies, also known as localized surface plasmon resonances (LSPRs).[1–6] The specific LSPR frequencies are known to be strongly dependent on NP shape, size and possibly crystallinity.[7] In Au NPs with anisotropic shapes, such as nanorods (NRs), different LSPR modes exist, associated with electron oscillations across (transverse LSPR) or along the NR long axis (longitudinal LSPR).[8–11] Plasmon resonances lead to strong absorption and scattering of the incident electromagnetic wave at the LSPR frequencies, with part of the absorbed energy being converted into heat through electron-

phonon relaxation. The generated heat is ultimately released to the surrounding medium. Heat generation is most efficiently controlled by excitation with femtosecond laser pulses, as energy absorption and electron-phonon scattering events are separated in time.[6,12–14] As a consequence of this photothermal effect, the local temperature can reach values high enough to induce reshaping of metal NPs.[14–22] Most interestingly, femtosecond laser pulses can also be used to selectively drive the tip-to-tip welding of Au NRs.[19,23–25] In a similar fashion to optical coupling of closely spaced NPs, welding leads to the formation of additional plasmon modes and potentially to strong field enhancements.[26–33] Because of these intriguing plasmonic properties, welded metal NRs are of great interest, with potential applications ranging from molecular sensing to nanoscale wave-guiding, where their plasmonic properties, such as the resonant energy and plasmon linewidth, play a major role.[34–37] Moreover, a tunable conductive junction in welded systems holds promise for active photonic devices such as ultrafast nanoswitches.[38] From a fundamental point of view, studying the plasmonic response of welded structures yields insight on electron transport at the nanoscale. Furthermore, welded structures can extend the plasmonic properties up to the mid-infrared.[33] To fully exploit these nanostructures in practical applications, it is crucial to understand the connection between the welding geometry and the resulting optical and structural properties.

The impact of femtosecond laser pulses on the welding of Au NRs has been explored using optical ensemble techniques such as absorbance measurements by UV/VIS/NIR spectroscopy, in combination with simulations.[31,32,39] Although transmission electron microscopy (TEM) has also been used for the characterization of welded nanostructures in previous studies, their main focus was the determination of the average aspect ratio of the NRs and the 2D projected geometry of welded NRs.[31,32] Consequently, the welding angles and dimensions of the nanojunctions could not be determined precisely. The 3D structure of welded NRs is therefore still to be revealed. Additionally, upon welding, defects may be introduced in the crystal

structure,[24] which have been shown to influence the physical properties of Au NPs.[7,40,41] For example, the presence of defects can lead to additional scattering of electrons,[42] resulting in damping of plasmon modes.[7] Unfortunately, it remains unclear what type of defects are introduced during welding under femtosecond laser pulse irradiation and a direct link between potentially induced structural defects and plasmonic properties is still lacking. In this study, we determined the 3D atomic structure of welded Au NRs with different welding geometries. Additionally, we analysed the energy and spatial distribution of plasmon modes for systems with different welding geometries, using electron energy loss spectroscopy in scanning transmission electron microscopy (STEM-EELS). Finally, to unravel the impact of defects on the plasmonic properties, welded NRs were investigated by STEM-EELS and compared to single-crystalline Au NRs at similar resonant energies.

RESULTS AND DISCUSSION

Welding of Au NRs was achieved by femtosecond laser pulses irradiation (see Materials and Methods for details), as reported by González-Rubio *et al.*[39] We focused primarily on tip-to-tip assembled Au NRs, which can be prepared by taking advantage of the higher reactivity of Au NRs tips compared to that of the sides towards their functionalization with dithiolated molecules. The assembly of Au NRs with LSPRs at 660 nm (Figure S1) results in dimers and trimers with LSPR modes located at *ca.* 800 nm, in resonance with the femtosecond laser pulses used in our experiments (see Materials and Methods for details). In addition, the assembly of Au NRs leads to the formation of hot spots at interparticle gaps. Thus, when the assembled Au NRs are irradiated with femtosecond laser pulses, the absorbed energy leads to an increment of the temperature of the nanocrystal lattice, resulting in increased mobility of the metal atoms constituting the irradiated Au NRs. Moreover, due to the higher curvature of the tips, the gold atoms located at such a position possess poorer coordination than those located at the sides,

which should further boost their mobility at high temperature. Besides, the shortest distances between the assembled Au NRs are at the tips, which together with the laser heating, and higher curvature of the tips may explain the observed tip-to-tip welding.[14–22] The approach also yields larger aggregates through assembly of dimers with each other or with other species (see Figure S1). Nevertheless, welded dimers and trimers are obtained in sufficiently high yield (between 10-20%)[39] to investigate the crystalline nature of the welded regions by electron tomography, as well as the impact of welding on the plasmonic properties at the single-particle level.

Figure 1 presents overview images acquired by high angle annular dark field scanning transmission electron microscopy (HAADF-STEM) of different dimer structures. These images show how the welded structures can yield a broad range of different geometries. However, these are two-dimensional projection images and the exact geometry and connection at the interface between the individual NRs should rather be investigated in three dimensions (3D).

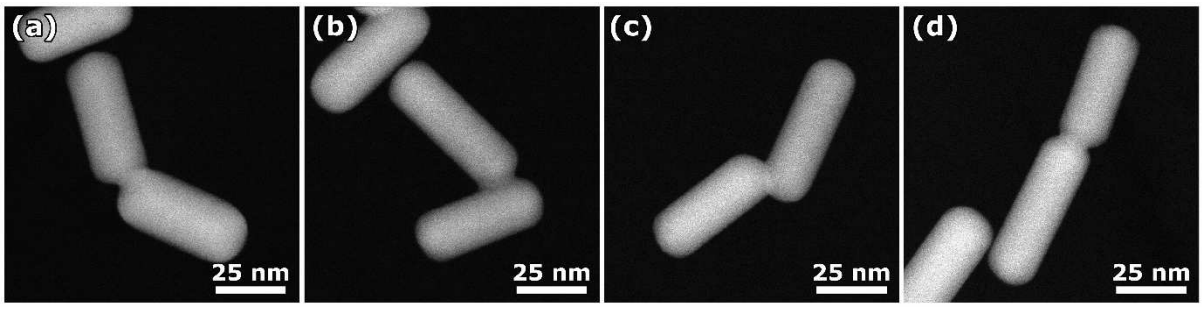

Figure 1. (a)-(d) HAADF-STEM images of different welded Au NRs.

Therefore, we applied electron tomography to study the morphologies obtained after laser welding. This technique is based on the acquisition of a tilt series of 2D HAADF-STEM images,[43,44] followed by 3D reconstruction using the simultaneous iterative reconstruction technique (SIRT).[45] Typical examples of 3D visualizations of the reconstructed volumes for different welding geometries are displayed in Figure 2a. From these data, we can determine the

welding angles in 3D and classify our welded nanostructures. In order to do so, one Au NR is oriented along the *z*-axis and two Euler angles α and β are defined around the *x* and *y* axes of an orthonormal reference (Figure 2b). Statistical 3D analysis of 32 configurations revealed that α ranges preferentially from 60º to 180º and β from 0º to 40º (Figure 2c,d). A similar distribution of α for NRs dimers and trimers connected by molecular linkers before welding was found in a previous report, albeit based on 2D images.[39] It should be noted, that our statistics based on 3D data sets are low compared to the 2D analysis performed there. Yet, the present results support the fact that the Au NRs maintain their initial orientation after welding under femtosecond laser pulse irradiation.

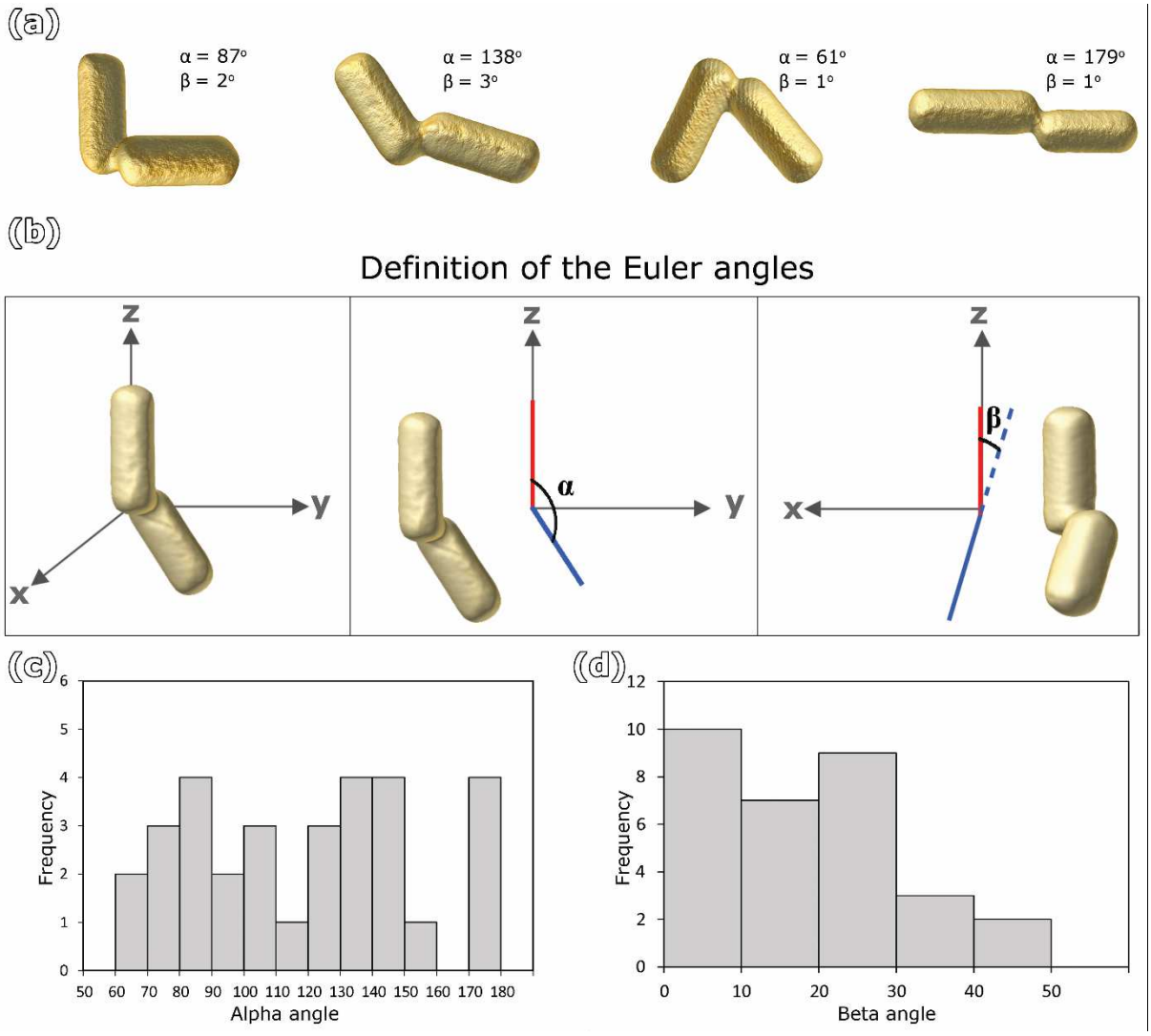

Figure 2. (a) 3D morphology of different welding geometries determined by electron tomography and their respective welding angles. (b) Definition of Euler angles: one Au NR is placed along the *z*-axis. α and β correspond to the angle of the other Au NR around the *y* and *x* axes, respectively. Statistical distribution of the welding angles (c) α and (d) β determined for 32 Au NR dimers with different configurations.

Most of the observed configurations, are likely to exhibit defects at the interface between the rods. This was confirmed by the high resolution HAADF-STEM images in Figure 3, suggesting two different types of defects, either dislocations or grain boundaries. We hypothesize that dislocations occurred when the 2 Au NRs had similar crystallographic orientations (Figure 3c,d) and grain boundaries otherwise (Figure 3a,b). Based on 2D high-resolution HAADF-STEM images, previous studies[39] have reported the presence of grain boundaries at the interface. However, since such HAADF-STEM images correspond to 2D projections of 3D objects, electron tomography experiments are crucial to obtain further understanding concerning the connection mechanism. More specifically, electron tomography enables one to unambiguously identify the defect type and to associate it with the 3D welding geometry of the system, which was still a challenge in previous studies.[39]

To prove our hypothesis on the origin of defect types, we performed electron tomography at the atomic level on two different systems, with the Au NRs being oriented along the same and different crystallographic orientations, respectively. Typically, either prior information about the investigated material or suitable constraints would be used to achieve atomic resolution in 3D.[46–48] These methods are unfortunately not applicable on the 3D investigation of more complex nanostructures such as the welded Au NRs in this study, as they could introduce bias in the results. Therefore, a recently developed methodology was implemented, in which prior information is no longer required thanks to the application of optimized acquisition and

alignment procedures.[49] This technique relies on the fast acquisition of multiple frames at every tilt angle, rather than one single image acquisition with a longer exposure time. In this manner, we were able to minimize slight rotations of the Au NRs during acquisition, which is a common problem when imaging NPs by HAADF-STEM at high magnification.[49] Scanning artefacts were corrected by means of a convolutional neural network (CNN) combined with rigid and non-rigid transformations.[49–52] Finally, a modified phase correlation approach was applied for the alignment of the tilt series. Further details of this procedure are provided in the Materials and Methods section.

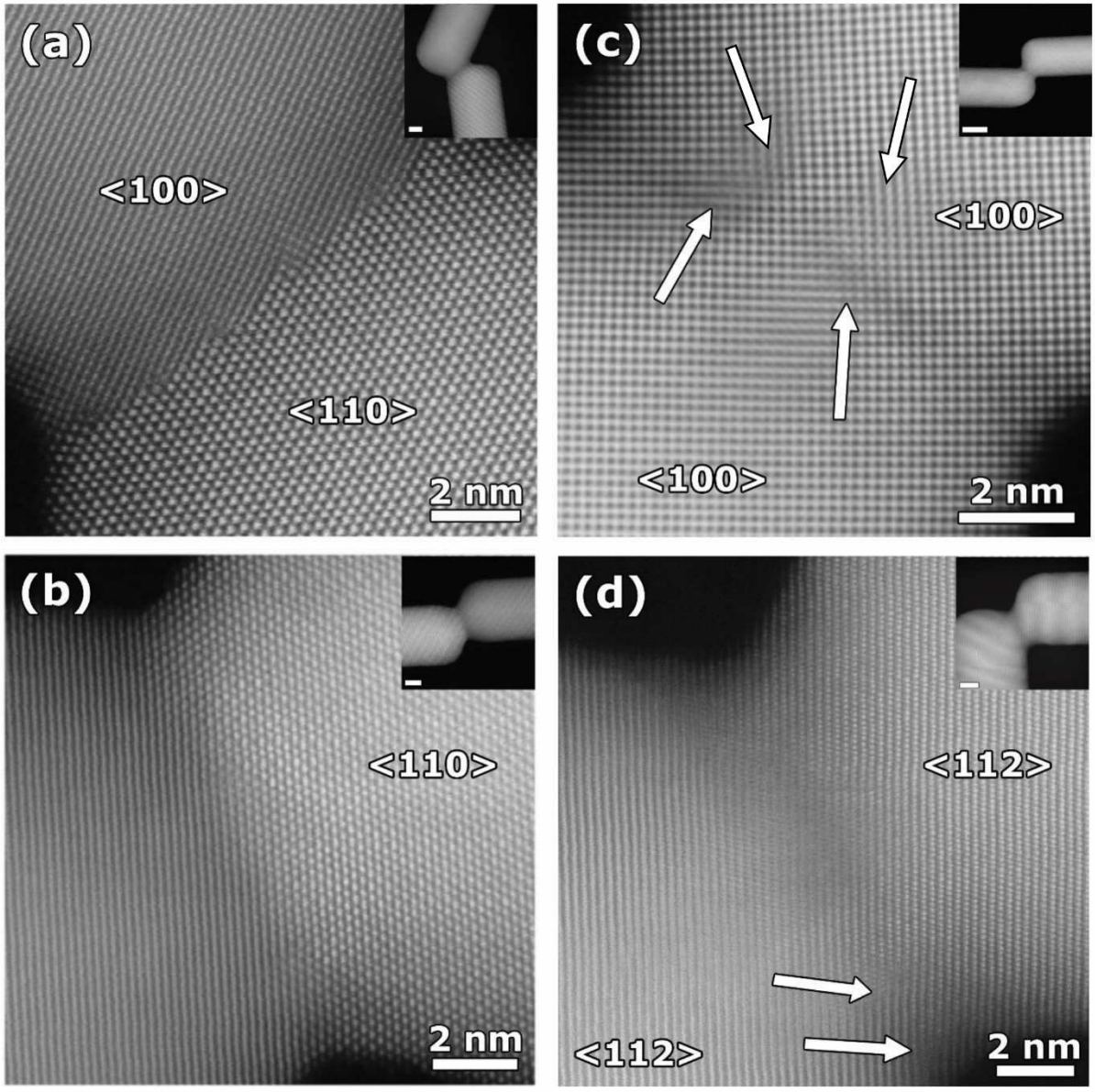

Figure 3. High-resolution HAADF-STEM images of welded Au NRs displaying different types of defects. The insets at the top right show lower magnification HAADF-STEM images (scale bars: 5 nm). The crystallographic orientations of Au NRs were obtained through the analysis of the FFT patterns (Figure S2). In panels (a,b), grain boundaries are observed at the interface between welded Au NRs, consistent with the different crystallographic orientations of the individual Au NRs, as indicated by the annotations. For welded Au NRs shown in (c,d), dislocations were found at the interface, as indicated by white arrows. Figure S3 displays a masked image where the visualization of the dislocation is clearer.

Using this approach, we first investigated a pair of Au NRs, exhibiting a welding angle α = 146º and a mismatch in crystallographic orientation between the two NRs. Figure 4a shows an overview image of the two connected Au NRs. A 3D representation of the reconstructed volume is shown in Figure 4b. This volume is limited to the connecting part of the NRs, allowing the acquisition of a tomography series with atomic resolution. Detailed analysis (Figure 4d-e) showed that these Au NRs did not have the same crystallographic orientation. The slice (e) was obtained after rotating slice (d) by an angle of 3º along the long axis of the welded Au NRs and an angle of 50º along the axis perpendicular to the slice. Moreover, further analysis of the 3D atomic structure revealed the presence of a grain boundary at the nanojunction. The result of manual segmentation of the defect throughout the 3D reconstruction is illustrated in Figure 4c. A similar analysis of another pair of welded Au NRs (α =131º) with a grain boundary at the interface yielded similar results (see Figure S4, Supporting Information).

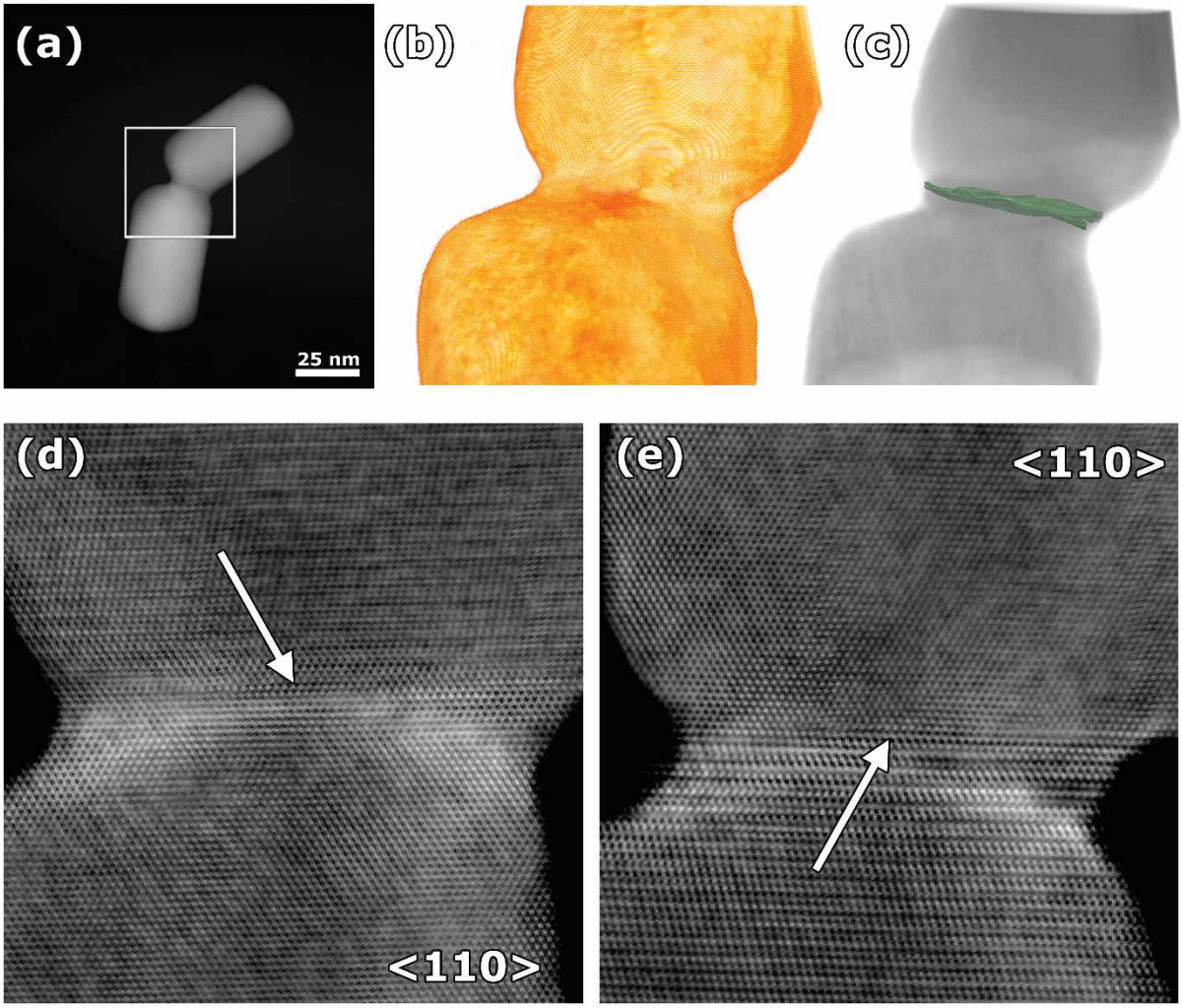

Figure 4. (a) Representative HAADF-STEM image of welded Au NRs with a grain boundary. The region inside the white box was studied by atomic resolution electron tomography. (b) 3D visualization of the reconstructed volume. (c) Segmented grain boundary. (d,e) Orthoslices through the 3D reconstruction, along different orientations, confirming the presence of a grain boundary. The white arrows in (d,e) indicate the plane where the defect is located. In panel (d) the left Au NR is oriented along the [110] zone axis, whereas in (e) the right Au NR is oriented along the [110] zone axis. Measurements of both crystallographic orientations revealed a rotational deviation of 3° and a tilt deviation of 50° between the Au NRs (as defined in Figure S5), which also correspond to the rotational operations between panels (d,e).

Next, a pair of Au NRs with similar crystallographic orientations was investigated. Figure 5 shows a trimer configuration with a welding angle α = 179º (Figure 5a) between the two upper NRs. Analysis of the 3D reconstruction (Figure 5b) revealed the presence of two dislocations at the interface (see orthoslice through the reconstruction in Figure 5c). The result of manual segmentation of the dislocations throughout the 3D reconstruction is depicted in Figure 5d. The left panel in Figure 5d displays the 3D extension of dislocation 1, which was found to cross the Au NRs following a non-parallel pathway with respect to the crystallographic planes. For dislocation 2 (right side of Figure 5d), a more irregular pattern was observed for the same defect.

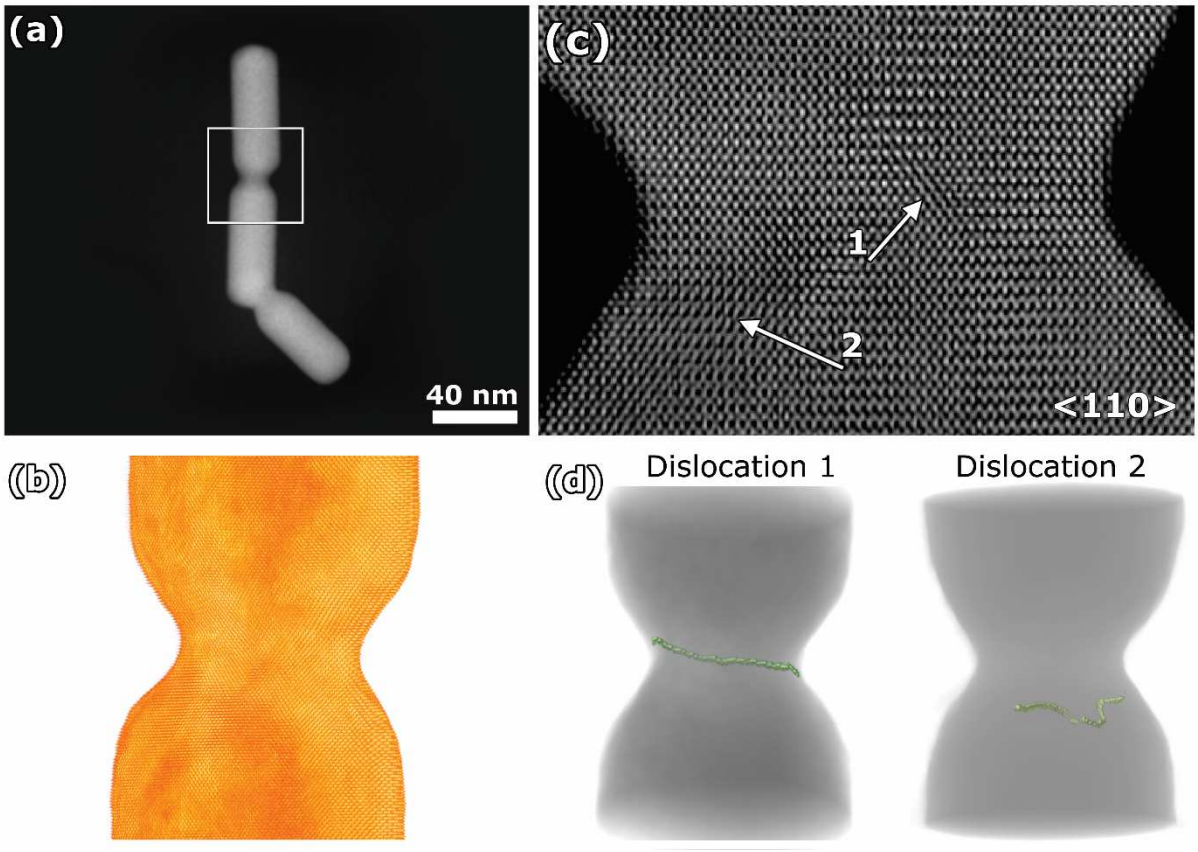

Figure 5. (a) HAADF-STEM image of a trimer of welded Au NRs. The region inside the white box was studied by high-resolution electron tomography. (b) Visualization of the 3D reconstructed volume. (c) Orthoslice through the 3D reconstruction revealing the presence of

two dislocations, highlighted by the white arrows 1 and 2, and a similar crystallographic orientation of the two NRs along the [110] zone axis. The identification of dislocations was performed in a similar manner as in Figure 3 and is demonstrated in Figure S6. (d) Dislocation 1 extends linearly through the interface, whereas dislocation 2 exhibits an irregular pattern.

Further analysis of 10 additional welded Au NR pairs confirmed the findings of Figures 4 and 5. Dislocations are mainly present at the interface for NRs with very similar crystallographic orientations. For all other cases, grain boundaries are present. More specifically, for gold based structures (FCC lattice), grain boundaries will be formed if the rotational angle ω and the tilt angle θ heavily deviates from ± nπ for a crystal oriented along [100] zone axis (Figure S5). These observations are of interest since the presence of defects may impact the dielectric function of the material[53–55], which can in turn influence the plasmonic properties of metal NPs. We therefore decided to further investigate the plasmonic properties of selected welded Au NR pairs and correlate them with the corresponding structural properties.

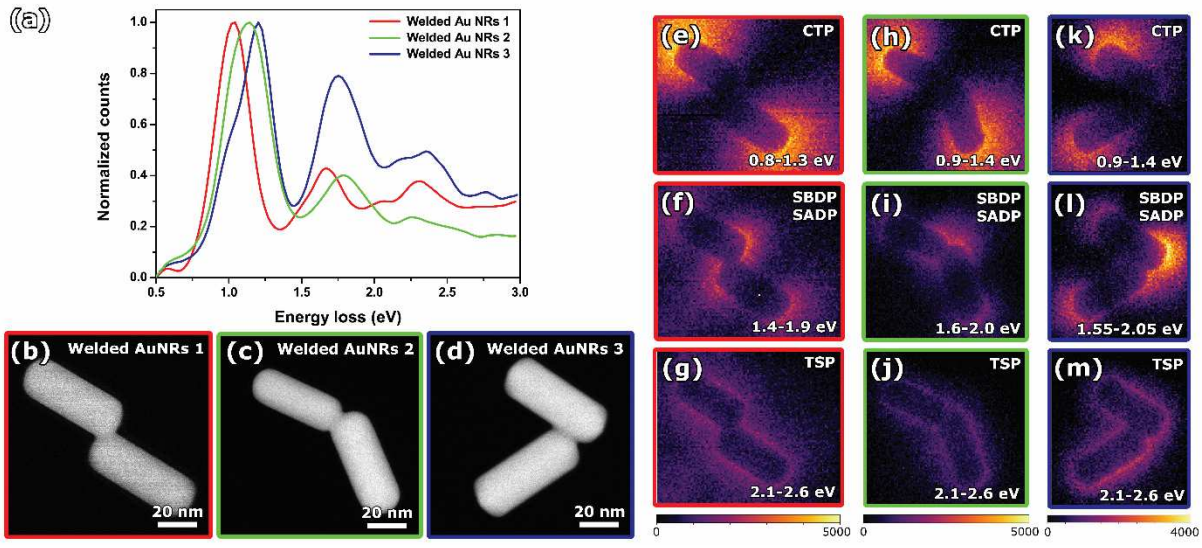

Figure 6. (a) Normalized EELS spectra of the three different welded NR pairs shown in panels (b)-(d). (e)-(m) Spatial distribution of the plasmon modes for the different welding geometries, selected from the spectra in (a). Three different plasmon modes were identified as CTP,

SBDP/SADP and TSP (see text for details). The energy range is indicated in each plasmon map.

When plasmonic NRs are placed in close proximity, a collective plasmonic behaviour arises from the capacitive coupling of the LSPR modes of each individual NR, giving rise to hybridized plasmon modes,[30,56] such as *e.g.*, the bonding dimer plasmon (BDP).[28,30,57] For a heterodimer with NRs of different aspect ratios, symmetry breaking leads to the anti-bonding dimer plasmon (ADP) mode being optically excitable as well.[58,59] The ADP is generally weaker in intensity than the BDP. Here, it should be noted that EELS is also sensitive to dark modes[60] and the ADP mode for almost identical coupled NRs can thus be observed by STEM-EELS.[61]

After welding, the presence of a conductive nanojunction between the Au NRs gives rise to an additional plasmon mode, associated with the charge flow between the Au NRs, known as the charge transfer plasmon (CTP) mode.[26,28,30,33] The BDP weakens and blue-shifts after welding due to the decreased capacitive coupling of the Au NRs and the interaction with the CTP mode.[62,63] This is referred to as the screened bonding dimer plasmon (SBDP) mode.[26–30,33,64] Simulations have shown that, in conductively connected heterodimers, a screened anti-bonding mode (SADP) at higher energies than the SBDP mode can also be observed as a bright mode, similar to the case of coupled but non-connected heterodimers.[29] Optical measurements and simulations have further revealed that for connected, as well as non-connected NR heterodimers, the bonding (anti-bonding) mode is governed by the longitudinal plasmon resonance of the NR with the higher (lower) aspect ratio.[29,58]. The main shortcoming of optical (single-particle) measurements is the lack of structural and geometrical correlation with high precision. For a complex system such as welded NRs, STEM-EELS is thus a valuable tool to correlate geometry, structure and plasmonic properties. We therefore proceeded to analyse the

plasmon modes and their spatial distribution for different welding geometries by monochromated STEM-EELS.

First, we looked at the spatial distribution of the different plasmon modes in three welded Au NR pairs with different welding angles α (Figure 6). Figure 6a shows STEM-EEL spectra acquired for all three welded pairs (Au NRs 1, 2, and 3), which are displayed in Figure 6b-d. The aspect ratios and sizes of the single NRs are very similar with only a slight variation between 2.5 and 2.7 (Table S1 in Supporting Information). On the basis of previous literature reports,[26–30,33,64] we identified three plasmon modes for each NP pair: the CTP mode at ~1 eV, the screened dimer plasmon mode (SBDP) at ~1.7 eV and the transverse surface plasmon (TSP) mode at ~2.3 eV. It should be noted that a small red-shift of the CTP mode was experimentally observed between the top and the bottom of the welded NR pair (Figure S7), resulting in slight broadening of the CTP peaks and in a lower energy shoulder for the CTP mode of welded NRs 3 (blue curve). Such a red-shift arises from the formation of an amorphous carbon layer during electron beam scanning, an unwanted effect referred to as "carbon contamination" in electron microscopy.[65–68] The carbon layer leads to an increase of the surrounding dielectric constant. Within our energy resolution, the screened dimer plasmon mode features a single peak with no splitting into bonding and anti-bonding modes. Indeed, since the NRs were of uniform morphology we would expect both modes to be degenerated.[29]

The spatial distributions of the three plasmon modes are shown in Figure 6e-m. As expected, the dipolar CTP mode exhibits an intense field concentration at the non-welded tips, whereas the TSP mode localizes along the lateral sides of the NRs. The SBDP/SADP mode exhibits a field concentration at both welded and non-welded tips, confirming that both bonding and anti-bonding modes are contributing. For the welded Au NRs 1, a rather uniform distribution was observed for all four tips. Please note that for this dimer, the upper NR has a slightly smaller

aspect ratio (2.5) than the lower one (2.7). Combined with the knowledge acquired from simulations, the differences in aspect ratio suggest that the field distribution around the lower (upper) NR is connected to the bonding (anti-bonding) mode.[29,58] Furthermore, a slightly higher field intensity appears at the non-welded end of the lower NR, compared to the upper NR, thus indicating a stronger contribution of the bonding mode. Although absolute EELS intensities need to be interpreted with caution, a stronger SBDP for connected NRs of similar size has been predicted by finite-element simulations.[29] Additionally, a higher field distribution is observed around the welded region compared to the non-welded tips, which becomes more dominant for the other two welding geometries (Figures 6i,l). This is likely related to the increased spatial overlap of the bonding and anti-bonding modes at the welded tips for decreasing α angles.

Interestingly, for the configuration with the lowest α angle (Figure 6l), the highest field concentration was not observed around the welded junction but at the welded tip of the upper NR. This observation indicates that this plasmon mode, which we attribute to the screened bonding mode, extends over the nanojunction. The observation fits well to simulation results[29] for connected Au NRs and could also explain the slightly red-shifted peak (1.77 eV) compared to welded Au NRs 2 (1.83 eV). Similar to the case of welded Au NRs 1, the bonding mode seems to be stronger than the anti-bonding mode. In addition, for the geometry of welded Au NRs 3, the SBDP/SABP mode exhibits higher intensity compared to that of the two geometries with larger α angles, as can be seen in the map (Figure 6l) and spectrum (Figure 6a, blue line). Our findings are consistent with the single-particle optical scattering measurements reported by Slaughter *et al.*[58] The authors observed an enhancement in the bonding dimer mode of touching Au NRs with an α angle of 140º, compared to that of straight touching dimers (α = 180º). However, the limited resolution of the scanning electron microscope that the authors used for the structural correlation hindered closer analysis of the correlation between the

particles' geometry and their scattering properties. Our work, offering a higher spatial resolution, corroborates their results.

An additional observation is that the spectral positions of the plasmon peaks differ in the three welded systems. Most notably, a blue-shift of the CTP from 1.0 eV (welded Au NR 1) to 1.1 eV (welded Au NR 2) and to 1.2 eV (welded Au NR 3) was observed. Since the NRs were very similar in size and aspect ratio, these variations are not expected to stem from geometry differences. This was confirmed by Boundary Element Method (BEM) simulations (Figure S8), assuming a straight alignment of Au NRs, as further detailed below. Indeed, the influence of the slightly different sizes is small as the CTP resonance energy only varies between 1.29 eV (welded Au NR 1) and 1.36 eV (welded Au NR 2). Moreover, the CTP resonance of welded Au NR 3 lies in-between welded Au NR 1 and 2. It is also known that the angle between connected or non-connected NRs barely influences the plasmon peak position.[32,58,59,69] However, it has been reported that the quality of the nanojunctions, often expressed in terms of conductance, may play a major role in the strength and the energy of the plasmon modes in connected Au NPs.[29–33,62,70] For the welded Au NR system, we performed additional simulations and observed that this is also true for our case, as displayed in Figure S9. For decreasing interface area, the CTP resonance red-shifts (a), gets weaker (b) and the linewidth decreases (c), in agreement with previous work.[33] Thus, the blue-shifted CTP resonance of welded Au NR 3 indicates that conductance at the interface is most likely better than for the other two welded Au NRs presented in Figure 6. In addition to the CTP mode, the observed features and differences for the SBDP/SADP mode may also be ascribed to a change in the geometry and size of the nanojunction.

We however realized that the correlation between structure and optical properties can be pushed even further. As revealed by the 3D structural characterization, all welded NRs exhibit

a defect at the nanojunction, either a grain boundary or a dislocation. Tang and Ouyang showed that defects can have a direct influence on the physical properties of NPs.[7] They fabricated single-crystalline and multi-twinned spherical Au NPs. By ensemble-averaged optical measurements they observed that the full-width at half-maximum (FWHM) of the plasmon peak was consistently 1.7 times larger for multi-twinned NPs than for single-crystalline NPs. Their work suggests that twinning defects play a critical role in damping and hence weakening of plasmon resonances. However, their particles exhibited a large amount of crystalline defects, which varied from particle to particle. So far, a direct link between crystal defects and plasmonic properties at the single-particle level of welded structures is still lacking. The welded NRs studied in this work are an excellent model system for such a correlation.

For this purpose, welded NR systems with almost identical welding geometry but different crystallographic orientations ($\alpha = 180^{\circ}$ and $\beta = 0^{\circ}$) were selected. Six pairs of welded Au NRs were investigated. Their sizes and (high resolution) STEM images are provided in the Supporting Information (Figures S10-S11 and Tables S1-S2). To study the influence of defects on the plasmonic properties, we determined the linewidth Γ of the CTP mode and compared it to that of the longitudinal resonance of single-crystalline Au NRs at similar resonant energies measured on the same TEM support during one TEM session and therefore using the exact same imaging parameters. Such a comparison is reasonable, because the CTP mode of welded Au NRs mimics the longitudinal mode of a single NR, which is larger in size and aspect ratio.[32] Our monochromated Themis Z electron microscope operated at 60 kV provided the energy resolution (< 100 meV), which is essential for such a comparison. The plasmon linewidth of the CTP mode was extracted from the deconvolved and zero-loss peak-subtracted spectrum, by fitting a Lorentzian function. Details of data acquisition and analysis are provided in the Materials and Methods section, while examples of two spectra, extracted in that way, are displayed in Figure 7a.

Figure 7b shows the obtained linewidths as a function of resonance energy. The CTP resonant energies of the six welded NRs systems (red dots) were close to each other, within the range 1.15 eV - 1.33 eV. Besides, high-resolution imaging revealed that grain boundaries were present at the interface of all welded Au NRs (Figure S11) displayed in Figure 7b. To compare the influence of defects on plasmon damping in systems without defects, single crystalline Au NRs with similar resonant energies and sizes as those of the welded systems were investigated under the same conditions. It is important to compare systems with and without defects at similar resonance energies to avoid variations in the plasmon linewidth due to changes in the dielectric function. Here, nine Au NRs with aspect ratios ranging from 4.0 to 7.1 were investigated, with resonant energies varying between 1.10 eV and 1.59 eV (see Figure S12-S13 and Table S2 in the Supporting Information for details). For these nine NRs (green dots in Figure 7b), Γ was found to increase with increasing resonance energy, as expected from previous literature and in agreement with BEM simulations (blue dots in Figure 7b), which will be detailed below.[71]

For the single-crystalline Au NRs, we measured a linewidth between 100 and 114 meV at an energy around 1.2-1.3 eV. However, the measured linewidth for the welded NR systems at the same resonance energies was 1.3-1.4 times larger, suggesting that a single grain boundary can be sufficient to induce significant plasmon broadening and hence damping. This hypothesis will be further discussed below.

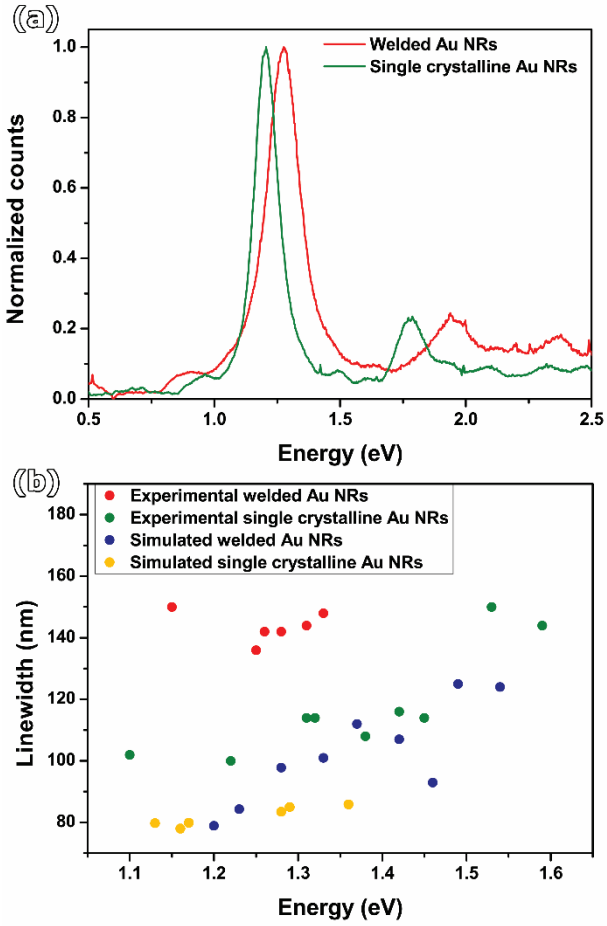

Figure 7. (a) EEL spectra of a welded Au NR (red) and a single-crystalline Au NR (green), where their Lorentzian character is evident. (b) Linewidth of the CTP mode for welded Au NRs (red), with almost identical welding geometry. Green dots represent the experimental values of the linewidth for different single-crystalline Au NRs with similar aspect ratio to the welded systems at varying resonant energies. Linewidths of the longitudinal mode for single-crystalline Au NRs (blue) and of the CTP mode for welded Au NRs (yellow) obtained from simulations, convoluted with the experimental energy resolution, are also displayed. For simulated welded nanostructures, smaller linewidths were observed in comparison with those for simulated single-crystalline Au NRs. This is likely associated with radiation damping, which scales with volume. Since the single-crystalline NRs have a slightly larger volume, they experience more radiation damping and hence exhibit greater broadening.

The presence of structural defects is responsible for locally changing the atomic potential of the object and, consequently, the dielectric function of the material.[72,73] In addition, for polycrystalline structures where the grain size is smaller than the mean-free path of the cloud of free electrons, an increase of the collision rate of free electrons with the boundary of the defect is expected.[74–76] Thus, an increase of the damping constant (characterized by the linewidth Γ) is observed for structures containing lattice defects, since the total damping term is the sum of the contribution of radiative and non-radiative internal processes, as well as the coupling of plasmonic modes with electronic transitions in the matrix in which the nanoparticle is embedded.[77–79] For non-radiative processes, contributions from the collision rate from electron-electron, electron-phonon and electron-defect scattering are the main parameters for metallic nanostructures.[75] A structural defect, such as a grain boundary as studied here, will lead to an increase in the collision rate of electrons and hence will broaden the plasmon resonance peak and reduce its intensity.

To verify our experimental results, we performed BEM simulations of Au NRs with the same dimensions and volumes as those of the 9 single-crystalline NRs (blue dots in Figure 7b), solving the full Maxwell's equations as implemented in the MNPBEM17 toolbox. [80–82] During the simulations, the effect of the limited resolution of the experimental data was included, through convolution of the simulated results with the experimental zero-loss peak (Figure S14 and Table S2). The effect of the convolution is more prominent for plasmonic modes with lower linewidths, as shown in Figure S15. Our analysis revealed a good agreement between simulated and experimental data for a surrounding dielectric constant of 1.4, which is higher than the dielectric constant of vacuum (that in a TEM experiment), likely due to the influence of the carbon substrate.

To exclude the possibility that the shape of welded NRs alone could cause such additional broadening, we also carried out simulations of welded NRs. In this case, the sizes of both Au NRs and the relative shift between them in the welded systems were determined from 2D images of welded NRs in the experiments (Figure S10), and later used as the input for simulations (Table S1-S3). The results are also shown in Figure 7b by the yellow dots. The calculated CTP resonance energies, between 1.16 eV and 1.36 eV, are in good agreement with the measured energies. The obtained linewidths varied between 78 meV and 86 meV, *i.e.* slightly below those for simulated single-crystalline Au NRs at similar resonance energies. This difference likely stems from the smaller volume of the welded Au NRs compared to the single-crystalline Au NRs, resulting in lower radiation damping.[83] These results strongly support our conclusion that the experimentally observed enhancement of plasmon damping stems from (single) crystal defects. Indeed, other studies have shown the effect of crystallographic defects on the plasmonic properties for lithographically fabricated polycrystalline nanostructures,[73,75,76,84,85] where the plasmon linewidth Γ after the annealing process, which contains a smaller density of defects, was found to be smaller when compared to non-thermally treated structures. More specifically, Chen and co-authors[75] have shown a decrease in the linewidth Γ of approximately 33% after thermal treatment at 400 °C. To specify, the induced plasmon broadening due to crystal defects is hence expected and has been measured for polycrystalline samples.[75,76] However, we show here that a single defect is enough to cause a significant plasmon broadening.

Our results offer valuable insights for the optimization of existing applications from molecular sensing to nanoscale wave-guiding, where plasmon broadening due to the presence of a single defect should be taken into consideration. In addition, narrow linewidths in the mid-infrared, as previously predicted[33], might not be as easily achievable, even when welding single-crystalline nanorods, as done here. An exciting future endeavor would therefore be to explore

options for healing defects in the welded nanostructures by *e.g.* thermal treatments, to achieve narrow linewidths in the near-IR and mid-IR.

CONCLUSIONS

In this study, we characterized the 3D (atomic) structure of welded Au NRs by electron tomography. For geometries of Au NRs with similar crystallographic orientations, dislocations were found at the interface, while all other geometries presented grain boundaries upon laser excitation. Moreover, investigation of the plasmonic properties of the welded Au NRs revealed damping of the CTP mode due to the presence of defects compared to the case of single-crystalline NRs at similar resonance energies. Not only do these results show the influence of defects on the plasmonic properties at the single Au NP level, confirming ensemble averaged predictions, but they also reveal that a single defect can have a significant impact on the plasmonic performance of metal NPs.

MATERIALS AND METHODS

Materials. All starting materials were obtained from commercial suppliers and used without further purification: Hexadecyltrimethylammonium bromide (CTAB, ≥99%), 5-bromosalicylic acid (technical grade, 90%), L-ascorbic acid (≥99%), sodium borohydride ($NaBH_4$, 99%), hydrogen tetrachloroaurate trihydrate ($HAuCl_4 \cdot H_2O$, ≥99.9%), silver nitrate ($AgNO_3$, ≥99.0%), 1,8-octanedithiol, branched polyethylenimine of average molecular weight of 25kDa (PEI), ammonium hydroxide solution (28.0-30.0% NH3), acetic anhydride (≥98.0%), methoxypolyethylene glycol maleimide (≥90%, MW 5.000) and ethanol (96%) were purchased from Aldrich. Nanopure water (resistivity 18.2 MΩ·cm at 25 °C) was used in all experiments.

Synthesis of Au NR: Au NRs were synthesized following the modified seed-mediated approach previously described by Scarabelli *et al.*:[86]

1–2 nm seeds: 25 μL of a 0.05 M $HAuCl_4$ solution was added to 4.7 mL of 0.1 M CTAB solution and stirred for 2 min until complete homogenization of the mixture. Then, 300 μL of a freshly prepared 0.01 M $NaBH_4$ solution was injected under vigorous stirring (1000 rpm). Excess borohydride was consumed by keeping the seed solution for 30 min at room temperature prior to use.

Au NRs with LSPRs at 660 nm: 45 mg of 5-bromosalicylic acid was added to 50 mL of 0.05 M CTAB and heated at 35 °C for 1 h. Then, 480 μL of 0.01 M $AgNO_3$ and 500 μL of 0.05 M $HAuCl_4$ solution were added to the mixture. After *ca.* 2 h at 25 °C, when the absorbance at 396 nm was reduced from *ca.* 1.2 to 0.2 (due to reduction of Au^{3+} to Au^{+}), 130 μL of a 0.1 M ascorbic acid solution was added under vigorous stirring. Finally, 80 μL of the 1–2 nm seed solution was injected under stirring and the mixture was left undisturbed at 25 °C for at least 4 h. The Au NRs were washed by centrifugation (6000 rpm, 30 min) and redispersed in 10 mL of a 2 mM CTAB solution. Analysis of the TEM images revealed Au NRs of 52 ± 4 nm and 21 ± 2 nm in length and width, respectively.

Single crystalline Au NRs: The Au NRs used for comparison of the plasmon linewidth in Figure 7 were synthesized following the method by Ye *et al.*[87]

Assembly and welding of Au NRs.

Transference to ethanol. Typically, 1 mL of 100 mg/mL aqueous solution of PEI was added dropwise to 4 mL of a Au NRs solution (2 mM CTAB, 5 mM Au) under vigorous stirring, which was left undisturbed for at least 2 h. The excess of free PEI was removed from the solution by a centrifugation cycle (3300 rpm, 30 min) and the NRs were redispersed in ethanol.

The concentration of gold was adjusted to 3.0–3.3 mM (*i.e.*, abs ~0.62 at 400 nm in a cuvette with 0.1 cm optical path).

Initiation of polymerization: 150 μL of an ethanol solution of PEI-stabilized Au NRs was mixed with 150 μL of a 1,8-octanedithiol ethanolic solution (0.5 mM to 0.1 mM, depending on the desired rate of polymerization) containing also 0.02% *v/v* of the ammonium hydroxide solution.

Termination: When the optical density at 800 nm matched that at 660 nm, the reaction was terminated by addition of 40 μL of acetic anhydride and 40 μL of a 25 mg/mL methoxypolyethylene glycol maleimide ethanol solution. Then, the reaction mixture was left to react for at least 30–60 min prior to irradiation with femtosecond laser pulses.

Irradiation with femtosecond laser pulses: 50-fs laser pulses were generated by an amplified Ti-Sapphire amplified laser system (Spectra Physics) centred at 804 nm and operating at a repetition rate of 1 kHz. The temporal profile of the 804 nm pulses was diagnosed by second harmonic autocorrelation. The fluence was fixed at 130 μJ/cm^2 through a variable attenuator wheel. Proper irradiation of the entire cuvette was ensured *via* scanning the cuvette with the laser beam using a mobile mirror. The polymerized Au NRs were irradiated (abs at 800 nm of *ca.* 1 in a quartz cuvette of 1 mm of optical pathlength) for 5 min and then centrifuged twice at 3000 rpm (10 min). Finally, the welded Au NRs were redispersed in 100 μL of ethanol.

Scanning transmission electron microscopy characterization. Low magnification and high-resolution HAADF-STEM images were acquired using a FEI-Osiris and an aberration-corrected 'cubed' FEI-Titan 60-300 electron microscopes operated at 200 and 300 kV, respectively. A diluted solution containing welded Au NRs (3μL) was drop-casted on a conventional TEM grid with a holey carbon support layer.

Conventional electron tomography. Tomography series were acquired using the Fischione model 2020 single-tilt tomography holder. The series were acquired over a tilt range from −72°

to +72°, with tilt increments of 2 or 3° and dwell time of 6 µs. The reconstruction of the tilt series was performed using the Astra Toolbox 1.8 for MATLAB 2018a.[88] The visualization of the 3D reconstructions was performed using the Amira 5.4.0 software.

Atomic resolution electron tomography. For acquisition of the atomic resolution tomography series, we recorded a time series for each projection with a fast acquisition scheme (dwell time of 0.4 µs). The series were acquired within a tilt range from −72° to +72°, with tilt increment of 2º. Next, a convolutional neural network (CNN) was applied in order to compensate for fast scan distortions, Gaussian and Poisson noise and jitter in the *x/y* directions[49]. Rigid and non-rigid transformation were applied to each time series for the correction of sample drift, shear and non-symmetrical artefacts generated during the acquisition.[49] An averaged image was then obtained for each projection. The tomography series was aligned with high accuracy, using a modified phase correlation procedure with subpixel precision.[49] Reconstruction of the 3D atomic structure was carried out using the SIRT algorithm, implemented in MATLAB 2018a. 3D visualizations were built in the Amira 5.4.0 software.

Tomographic reconstructions were performed using a workstation equipped with a Nvidia GeForce GTX Titan Black (6 GB of memory) graphical card, Intel (R) Core (TM) i7-4930 CPU @ 3.40 GHz processor and 64 GB of RAM. Typical running times were about 5 minutes for low magnification data (512 x 512 pixels) and about 90 minutes for atomic resolution data (1024 x 1024 pixels).

Electron energy loss spectroscopy. Low loss spectrum maps for the characterization of the plasmonic properties were acquired in a monochromated aberration-corrected 'cubed' FEI-Titan 60-300 electron microscope operated at 120 kV with energy resolution of 175 meV.

The spectrum maps to evaluate the impact of defects on the plasmonic properties were acquired in a monochromated aberration-corrected 'cubed' ThermoFischer Themis Z 60-300 electron

microscope operated at 60 kV with an energy resolution of 90 meV and a dispersion of 0.002 eV/channel.

HyperSpy 1.5.2[89] was used for the analysis of all EELS data. After alignment and subsequent removal of the zero-loss peak, the EEL spectra were deconvolved using the implemented Richardson-Lucy deconvolution with 15 iterations. The EEL spectra in Figure 6a are the summed deconvolved spectra. The corresponding maps were obtained for the given energy range. To extract the plasmon linewidth, the CTP spectra were extracted at the tip of the NP closest to the top region of the scanned area, to ensure that no carbon build-up artificially broadened the plasmon mode.[66–68] Next, the spectra were fitted using the Lorentzian line shape: $I\frac{(\Gamma/2)^2}{(x-x_0)^2+(\Gamma/2)^2}$

where I is the intensity, x_0 is the resonance energy and Γ is the linewidth.

BEM simulations. Simulations were carried out in the MNPBEM 17 Toolbox[80–82] using the full Maxwell equations. The system was excited by a plane wave with polarization direction along the *z* axis. The long axes of the input NRs were also oriented along this direction. The dielectric function of the surrounding medium was ε = 1.4, mimicking the effect of the carbon support. The dimensions of the NRs used for the simulations are shown in Table S2. The volumes of the NRs were estimated from the 2D projection images. For welded NRs, the second NR was shifted in the x and z directions with respect to the first NR, to resemble the experimental system. The values of the shifts can be found in Table S3.

ASSOCIATED CONTENT

Supporting Information. Additional material is provided: UV-VIS spectra of Au NRs during and after femtosecond laser pulses irradiation; TEM images of assembled Au NRs before and after welding; high resolution STEM images of defects before and after Fourier filtering to

enhance the visualization of dislocations; tomographic reconstruction at the atomic level of the connection region of the welded Au NRs; definition of tilt and rotational deviation from perfect epitaxy between two crystals; EELS spectra of the CTP mode extracted from the upper and lower non-welded tips; simulation of extinction cross section for welded Au NRs with straight alignment; analysis of the influence of the interface size between welded Au NRs; low and high magnification HAADF-STEM images of single crystalline Au NRs and welded Au NRs investigated by EELS; simulation of the linewidths for single crystalline Au NRs before and after convolution with the experimental zero loss peak; and tables containing the length, width, the simulated linewidth before and after convolution of single crystalline Au NRs and welded Au NRs; table containing the relative shifts in x and z directions between welded Au NRs.This material is available free of charge *via* the Internet at https://pubs.acs.org/

AUTHOR INFORMATION

Corresponding Author

Email: Sara.Bals@uantwerpen.be; Wiebke.Albrecht@uantwerpen.be

Author Contributions

‡These authors contributed equally.

ACKNOWLEDGEMENTS

This project has received funding from the European Research Council under the European Union's Horizon 2020 research and innovation program (ERC Consolidator Grants #815128 – REALNANO and #770887 - PICOMETRICS). The authors gratefully acknowledge funding from the Research Foundation Flanders (FWO, Belgium) through project funding G.0381.16N and G.0267.18N. W.A. acknowledges an Individual Fellowship funded by the Marie

Sklodowska-Curie Actions (MSCA) in Horizon 2020 program (grant 797153, SOPMEN). G.G.-R. acknowledge receipt of FPI Fellowship from the Spanish MINECO. This work has been funded by the Spanish Ministry of Science, Innovation and Universities (MICIU) (Grants RTI2018-095844-B-I00 and MAT2017-86659-R) and the Madrid Regional Government (Grant P2018/NMT-4389). A.B. acknowledges funding from FWO project G093417N and from the European Union's Horizon 2020 research and innovation programme under grant agreement No 823717 – ESTEEM3. L.M.L.-M. acknowledges the Maria de Maeztu Units of Excellence Program from the Spanish State Research Agency (Grant No. MDM-2017-0720).

REFERENCES

(1) Link, S.; El-Sayed, M. A. Shape and Size Dependence of Radiative, Non-Radiative and Photothermal Properties of Gold Nanocrystals. *Int. Rev. Phys. Chem.* **2000**, *19*, 409–453.

(2) Elahi, N.; Kamali, M.; Baghersad, M. H. Recent Biomedical Applications of Gold Nanoparticles: A Review. *Talanta* **2018**, *184*, 537–556.

(3) Hutchings, G. J.; Edwards, J. K. Application of Gold Nanoparticles in Catalysis. *Front. Nanosci.* **2012**, *3*, 249–293.

(4) Hvolbæk, B.; Janssens, T. V. .; Clausen, B. S.; Falsig, H.; Christensen, C. H.; Nørskov, J. K. Catalytic Activity of Au Nanoparticles. *Nano Today* **2007**, *2*, 14–18.

(5) Baffou, G.; Quidant, R. Thermo-Plasmonics: Using Metallic Nanostructures as Nano-Sources of Heat. *Laser Photonics Rev.* **2013**, *7*, 171–187.

(6) Pyatenko, A.; Wang, H.; Koshizaki, N.; Tsuji, T. Mechanism of Pulse Laser

Interaction with Colloidal Nanoparticles. *Laser Photonics Rev.* **2013**, *7*, 596–604.

(7) Tang, Y.; Ouyang, M. Tailoring Properties and Functionalities of Metal Nanoparticles through Crystallinity Engineering. *Nat. Mater.* **2007**, *6*, 754–759.

(8) Pérez-Juste, J.; Pastoriza-Santos, I.; Liz-Marzán, L. M.; Mulvaney, P. Gold Nanorods: Synthesis, Characterization and Applications. *Coord. Chem. Rev.* **2005**, *249*, 1870–1901.

(9) Chen, H.; Shao, L.; Li, Q.; Wang, J. Gold Nanorods and Their Plasmonic Properties. *Chem. Soc. Rev.* **2013**, *42*, 2679–2724.

(10) Payne, E. K.; Shuford, K. L.; Park, S.; Schatz, G. C.; Mirkin, C. A. Multipole Plasmon Resonances in Gold Nanorods. *J. Phys. Chem. B* **2006**, *110*, 2150–2154.

(11) Vigderman, L.; Khanal, B. P.; Zubarev, E. R. Functional Gold Nanorods : Synthesis , Self-Assembly , and Sensing Applications. *Adv. Mater.* **2012**, *24*, 4811–4841.

(12) Letfullin, R. R.; George, T. F.; Duree, G. C.; Bollinger, B. M. Ultrashort Laser Pulse Heating of Nanoparticles : Comparison of Theoretical Approaches. *Adv. Opt. Technol.* **2008**, Article ID 251718.

(13) Romanov, O. G.; Zheltov, G. I.; Romanov, G. S. Action of Femtosecond Laser Pulses on Metal Nanoparticles in a Liquid. *Bull. Russ. Acad. Sci. Phys.* **2011**, *75*, 1589–1591.

(14) Falamas, A.; Tosa, N.; Tosa, V. Dynamics of Laser Excited Colloidal Gold Nanoparticles Functionalized with Cysteine Derivatives. *J. Quant. Spectrosc. Radiat. Transf.* **2015**, *162*, 207–212.

(15) Kurita, H.; Takami, A.; Koda, S. Size Reduction of Gold Particles in Aqueous Solution

by Pulsed Laser Irradiation. *Appl. Phys. Lett.* **1998**, *72*, 789–791.

(16) Yamada, K.; Miyajima, K.; Mafuné, F. Thermionic Emission of Electrons from Gold Nanoparticles by Nanosecond Pulse-Laser Excitation of Interband. *J. Phys. Chem. C* **2007**, *111*, 11246–11251.

(17) Takami, A.; Kurita, H.; Koda, S. Laser-Induced Size Reduction of Noble Metal Particles. *J. Phys. Chem. B* **1999**, *103*, 1226–1232.

(18) González-Rubio, G.; Díaz-Núñez, P.; Rivera, A.; Prada, A.; Tardajos, G.; González-Izquierdo, J.; Bañares, L.; Llombart, P.; Macdowell, L. G.; Palafox, M. A.; Liz-Marzán, L. M.; Peña-Rodríguez, O.; Guerrero-Martínez, A. Femtosecond Laser Reshaping Yields Gold Nanorods with Ultranarrow Surface Plasmon Resonances. *Science.* **2017**, *358*, 640–644.

(19) Chang, S.-S.; Shih, C.-W.; Chen, C.-D.; Lai, W. C.; Wang, C. R. C. The Shape Transition of Gold Nanorods. *Langmuir* **1999**, *15*, 701–709.

(20) Link, S.; Burda, C.; Mohamed, M. B.; Nikoobakht, B.; El-Sayed, M. A. Laser Photothermal Melting and Fragmentation of Gold Nanorods: Energy and Laser Pulse-Width Dependence. *J. Phys. Chem. A* **1999**, *103*, 1165–1170.

(21) Link, S.; Burda, C.; Nikoobakht, B.; El-Sayed, M. A. Laser-Induced Shape Changes of Colloidal Gold Nanorods Using Femtosecond and Nanosecond Laser Pulses. *J. Phys. Chem. B* **2000**, *104*, 6152–6163.

(22) Liu, D.; Li, C.; Zhou, F.; Zhang, T.; Zhang, H.; Li, X.; Duan, G.; Cai, W.; Li, Y. Rapid Synthesis of Monodisperse Au Nanospheres through a Laser Irradiation-Induced Shape Conversion, Self-Assembly and Their Electromagnetic Coupling SERS

Enhancement. *Sci. Rep.* **2015**, *5*, 1–9.

(23) Fales, A. M.; Vogt, W. C.; Pfefer, J.; Ilev, I. K. Quantitative Evaluation of Nanosecond Pulsed Laser-Induced Photomodification of Plasmonic Gold Nanoparticles. *Sci. Rep.* **2017**, *7*, 1–11.

(24) González-Rubio, G.; Guerrero-Martínez, A.; Liz-Marzán, L. M. Reshaping, Fragmentation, and Assembly of Gold Nanoparticles Assisted by Pulse Lasers. *Acc. Chem. Res.* **2016**, *49*, 678–686.

(25) Albrecht, W.; Deng, T. S.; Goris, B.; Van Huis, M. A.; Bals, S.; Van Blaaderen, A. Single Particle Deformation and Analysis of Silica-Coated Gold Nanorods before and after Femtosecond Laser Pulse Excitation. *Nano Lett.* **2016**, *16*, 1818–1825.

(26) Zhang, H.; Chun, L.; Zhang, C.; Zhang, X.; Gu, J.; Jin, B.; Han, J.; Zhang, W. Experimental Study on the Transition of Plasmonic Resonance Modes in Double-Ring Dimers by Conductive Junctions in the Terahertz Regime. *Opt. Express* **2016**, *24*, 27415–27422.

(27) Koya, A. N.; Lin, J. Bonding and Charge Transfer Plasmons of Conductively Bridged Nanoparticles: The Effects of Junction Conductance and Nanoparticle Morphology. *J. Appl. Phys.* **2016**, *120*, 093105.

(28) Koya, A. N.; Lin, J. Charge Transfer Plasmons: Recent Theoretical and Experimental Developments. *Appl. Phys. Rev.* **2017**, *4*, 021104.

(29) Zhang, M.; Qi, J.; Jiang, M.; Li, Y.; Qian, J.; Chen, J.; Chen, Z.; Sun, Q.; Xu, J. Screened Bonding , Antibonding and Charge Transfer Plasmon Modes in Conductively Connected Nanorod Heterodimer. *J. Opt.* **2018**, *20*, 025001.

(30) Perez-Gonzalez, O.; Zabala, N.; Aizpurua, J. Optical Characterization of Charge Transfer and Bonding Dimer Plasmons in Linked Interparticle Gaps. *New J. Phys.* **2011**, *13*, 083013.

(31) Fontana, J.; Ratna, B. R. Highly Tunable Gold Nanorod Dimer Resonances Mediated through Conductive Junctions. *Appl. Phys. Lett.* **2014**, *105*, 011107.

(32) Fontana, J.; Charipar, N.; Flom, S. R.; Naciri, J.; Pique, A.; Ratna, B. R. Rise of the Charge Transfer Plasmon : Programmable Concatenation of Conductively Linked Gold Nanorod Dimers. *ACS Photonics* **2016**, *5*, 904–911.

(33) Wen, F.; Zhang, Y.; Gottheim, S.; King, N. S.; Zhang, Y.; Nordlander, P.; Halas, N. J. Charge Transfer Plasmons: Optical Frequency Conductances and Tunable Infrared Resonances. *ACS Nano* **2015**, *9*, 6428–6435.

(34) Haidar, I.; Lévi, G.; Mouton, L.; Aubard, J.; Grand, J.; Lau-Truong, S.; Neuville, D. R.; Félidj, N.; Boubekeur-Lecaque, L. Highly Stable Silica-Coated Gold Nanorods Dimers for Solution-Based SERS. *Phys. Chem. Chem. Phys.* **2016**, *18*, 32272–32280.

(35) Haidar, I.; Aubard, J.; Lévi, G.; Lau-Truong, S.; Mouton, L.; Neuville, D. R.; Félidj, N.; Boubekeur-Lecaque, L. Design of Stable Plasmonic Dimers in Solution: Importance of Nanorods Aging and Acidic Medium. *J. Phys. Chem. C* **2015**, *119*, 23149–23158.

(36) Osberg, K. D.; Rycenga, M.; Harris, N.; Schmucker, A. L.; Langille, M. R.; Schatz, G. C.; Mirkin, C. A. Dispersible Gold Nanorod Dimers with Sub-5 Nm Gaps as Local.Pdf. *Nano Lett.* **2012**, *12*, 3828–3832.

(37) Funston, A. M.; Novo, C.; Davis, T. J.; Mulvaney, P. Plasmon Coupling of Gold

Nanorods at Short Distances and in Different Geometries. *Nano Lett.* **2009**, *9*, 1651–1658.

(38) Large, N.; Abb, M.; Aizpurua, J.; Muskens, O. L. Photoconductively Loaded Plasmonic Nanoantenna as Building Block for Ultracompact Optical Switches. *Nano Lett.* **2010**, *10*, 1741–1746.

(39) González-Rubio, G.; González-Izquierdo, J.; Bañares, L.; Tardajos, G.; Rivera, A.; Altantzis, T.; Bals, S.; Peña-Rodríguez, O.; Guerrero-Martínez, A.; Liz-Marzán, L. M. Femtosecond Laser-Controlled Tip-To-Tip Assembly and Welding of Gold Nanorods. *Nano Lett.* **2015**, *15*, 8282–8288.

(40) Huang, W.; Qian, W.; El-Sayed, M. A. Effect of the Lattice Crystallinity on the Electron−Phonon Relaxation Rates in Gold Nanoparticles. *J. Phys. Chem. C* **2007**, *111*, 10751–10757.

(41) Hartland, G. V. Optical Studies of Dynamics in Noble Metal Nanostructures. *Chem. Rev.* **2011**, *111*, 3858–3887.

(42) Lormand, G. Electrical Properties of Grain Boundaries. *J. Phys. Coloques* **1982**, *43*, C6-283-C6-292.

(43) Midgley, P. A.; Bals, S. Electron Tomography. In *Handbook of Nanoscopy*; Van Tendeloo, G., Van Dyck, D., Pennycook, S. J., Eds.; Wiley-VCH: Weinheim, Germany, 2012; pp 253–279.

(44) Weyland, M.; Midgley, P. A. Electron Tomography. *Mater. Today* **2004**, *7*, 32–40.

(45) Palenstijn, W. J.; Batenburg, K. J.; Sijbers, J. Performance Improvements for Iterative Electron Tomography Reconstruction Using Graphics Processing Units (GPUs). *J.*

Struct. Biol. **2011**, *176*, 250–253.

(46) Aert, S. Van; Batenburg, K. J.; Rossell, M. D.; Erni, R.; Tendeloo, G. Van. Three-Dimensional Atomic Imaging of Crystalline Nanoparticles. *Nature* **2011**, *470*, 374–377.

(47) Goris, B.; Bals, S.; Broek, W. Van Den; Carbó-Argibay, E.; Gómez-Graña, S.; Liz-Marzán, L. M.; Tendeloo, G. Van. Atomic-Scale Determination of Surface Facets in Gold Nanorods. *Nat. Mater.* **2012**, *11*, 930–935.

(48) Goris, B.; Beenhouwer, J. De; Backer, A. De; Zanaga, D.; Batenburg, K. J.; Sanchez-Iglesias, A.; Liz-marza, L. M.; Van Aert, S.; Bals, S.; Sijbers, J.; Van Tendeloo, G. Measuring Lattice Strain in Three Dimensions through Electron Microscopy. *Nano Lett.* **2015**, *15*, 6996–7001.

(49) Altantzis, T.; Lobato, I.; Backer, A. De; Beche, A.; Zhang, Y.; Basak, S.; Porcu, M.; Xu, Q.; Sanchez-Iglesias, A.; Liz-Marzán, L. M.; Van Tendeloo, G.; Van Aert, S.; Bals, S. Three-Dimensional Quantification of the Facet Evolution of Pt Nanoparticles in a Variable Gaseous Environment. *Nano Lett.* **2019**, *19*, 477–481.

(50) Jones, L.; Yang, H.; Pennycook, T. J.; Marshall, M. S. J.; Aert, S. Van; Browning, N. D.; Castell, M. R.; Nellist, P. D. Smart Align - A New Tool for Robust Non-Rigid Registration of Scanning Microscope Data. *Adv. Struct. Chem. Imaging* **2015**, *1*, 1–16.

(51) Berkels, B.; Binev, P.; Blom, D. A.; Dahmen, W.; Sharpley, R. C.; Vogt, T. Optimized Imaging Using Non-Rigid Registration. *Ultramicroscopy* **2014**, *138*, 46–56.

(52) Yankovich, A. B.; Zhang, C.; Oh, A.; Slater, T. J. A.; Azough, F.; Freer, R.; Haigh, S. J.; Willett, R.; Voyles, P. M. Non-Rigid Registration and Non-Local Principle

Component Analysis to Improve Electron Microscopy Spectrum Images. *Nanotechnology* **2016**, *27*, 364001.

(53) Singh, S.; Khare, N. Effect of Intrinsic Strain on the Optical Bandgap and Magnetic Properties of Single Domain - CoFe2O4 Nanoparticles. *Appl. Phys. A* **2018**, *124*, 107.

(54) Yang, L.; Cui, X.; Zhang, J.; Wang, K.; Shen, M.; Zeng, S.; Dayeh, S. A.; Feng, L.; Xiang, B. Lattice Strain Effects on the Optical Properties of MoS2 Nanosheets. *Sci. Rep.* **2014**, *4*, 5949.

(55) Dhara, S.; Imakita, K.; Giri, P. K.; Fujii, M. Strain Dependence of the Nonlinear Optical Properties of Strained Si Nanoparticles. *Opt. Lett.* **2014**, *39*, 3833–3836.

(56) Willingham, B.; Brandl, D. W.; Nordlander, P. Plasmon Hybridization in Nanorod Dimers. *Appl. Phys. B Lasers Opt.* **2008**, *93*, 209–216.

(57) Jain, P. K.; Eustis, S.; El-sayed, M. A. Plasmon Coupling in Nanorod Assemblies : Optical Absorption , Discrete Dipole Approximation Simulation , and Exciton-Coupling Model. *J. Phys. Chem. B* **2006**, *110*, 18243–18253.

(58) Slaughter, L. S.; Wu, Y.; Willingham, B. A.; Nordlander, P.; Link, S. Effects of Symmetry Breaking and Conductive Contact on the Plasmon Coupling in Gold Nanorod Dimers. *ACS Nano* **2010**, *4*, 4657–4666.

(59) Shao, L.; Woo, K. C.; Chen, H.; Jin, Z.; Wang, J.; Lin, H. Angle- and Energy-Resolved Plasmon Coupling in Gold Nanorod Dimers. *ACS Nano* **2010**, *4*, 3053–3062.

(60) Myroshnychenko, V.; Nelayah, J.; Adamo, G.; Geuquet, N.; Rodrígues-Fernández, J.; Pastoriza-Santos, I.; Macdonald, K. F.; Henrard, L.; Liz-marza, L. M.; Zheludev, N. I.; Kociak, M.; Abajo, F. J. G. de. Plasmon Spectroscopy and Imaging of Individual Gold

Nanodecahedra: A Combined Optical Microscopy, Cathodoluminescence, and Electron Energy-Loss Spectroscopy Study. *Nano Lett.* **2012**, *12*, 4172–4180.

(61) Chu, M. W.; Myroshnychenko, V.; Chen, C. H.; Deng, J. P.; Niou, C. Y.; De Abajo, F. J. G. Probing Bright and Dark Surface-Plasmon Modes in Lndividual and Coupled Noble Metal Nanoparticles Using an Electron Beam. *Nano Lett.* **2009**, *9*, 399–404.

(62) Perez-Gonzalez, O.; Zabala, N.; Bosisov, A. G.; Halas, N. J.; Nordlander, P.; Aizpurua, J. Optical Spectroscopy of Conductive Junctions in Plasmonic Cavities. *Nano Lett.* **2010**, *10*, 3090–3095.

(63) Liu, L.; Wang, Y.; Fang, Z.; Zhao, K. Plasmon Hybridization Model Generalized to Conductively Bridged Nanoparticle Dimers. *J. Chem. Phys.* **2013**, *139*, 064310.

(64) Lerch, S.; Reinhard, B. M. Effect of Interstitial Palladium on Plasmon-Driven Charge Transfer in Nanoparticle Dimers. *Nat. Commun.* **2018**, *9*, 1608.

(65) Reimer, L.; Kohl, H. Specimen Damage by Electron Radiation. *Transmission Electron Microscopy: Physics of Image Formation*, Fifth edition.; Springer: New York, 2008.

(66) Albrecht, W.; van de Glind, A.; Yoshida, H.; Isozaki, Y.; Imhof, A.; van Blaaderen, A.; de Jongh, P. E.; de Jong, K. P.; Zečević, J.; Takeda, S. Impact of the Electron Beam on the Thermal Stability of Gold Nanorods Studied by Environmental Transmission Electron Microscopy. *Ultramicroscopy* **2018**, *193*, 97–103.

(67) Griffiths, A. J. V.; Walther, T. Quantification of Carbon Contamination under Electron Beam Irradiation in a Scanning Transmission Electron Microscope and Its Suppression by Plasma Cleaning. *J. Phys. Conf. Ser.* **2010**, *241*, 012017.

(68) McGilvery, C. M.; Goode, A. E.; Shaffer, M. S. P.; McComb, D. W. Contamination of

Holey/Lacey Carbon Films in STEM. *Micron* **2012**, *43*, 450–455.

(69) Kumar, J.; Wei, X.; Barrow, S.; Funston, A. M.; Thomas, K. G.; Mulvaney, P. Surface Plasmon Coupling in End-To-End Linked Gold Nanorod Dimers and Trimers. *Phys. Chem. Chem. Phys.* **2013**, *15*, 4258–4264.

(70) Romero, I.; Aizpurua, J.; Bryant, G. W.; García De Abajo, F. J. Plasmons in Nearly Touching Metallic Nanoparticles: Singular Response in the Limit of Touching Dimers. *Opt. Express* **2006**, *14*, 9988.

(71) Hoggard, A.; Wang, L. Y.; Ma, L.; Fang, Y.; You, G.; Olson, J.; Liu, Z.; Chang, W. S.; Ajayan, P. M.; Link, S. Using the Plasmon Linewidth to Calculate the Time and Efficiency of Electron Transfer Between Gold Nanorods and Graphene. *ACS Nano* **2013**, *7*, 11209–11217.

(72) Kittel, C. *Introduction to Solid State Physics*, Eighth edition; John Wiley & Sons, Inc.: United States of America, 2005.

(73) Tinguely, J. C.; Sow, I.; Leiner, C.; Grand, J.; Hohenau, A.; Felidj, N.; Aubard, J.; Krenn, J. R. Gold Nanoparticles for Plasmonic Biosensing: The Role of Metal Crystallinity and Nanoscale Roughness. *Bionanoscience* **2011**, *1*, 128–135.

(74) Ni, G.; McLeod, A.; Sun, Z.; Wang, L.; Xiong, L.; Post, K.; Sunku, S.; Jiang, B.; Hone, J.; Dean, C.; Fogler, M.; Basov, D. Fundamental Limits to Graphene Plasmonics. *Nature* **2018**, *557*, 530–533.

(75) Chen, K. P.; Drachev, V. P.; Borneman, J. D.; Kildishev, A. V.; Shalaev, V. M. Drude Relaxation Rate in Grained Gold Nanoantennas. *Nano Lett.* **2010**, *10*, 916–922.

(76) Tauzin, L. J.; Cai, Y. Y.; Smith, K. W.; Hosseini Jebeli, S. A.; Bhattacharjee, U.;

Chang, W. S.; Link, S. Exploring the Relationship between Plasmon Damping and Luminescence in Lithographically Prepared Gold Nanorods. *ACS Photonics* **2018**, *5*, 3541–3549.

(77) Kolwas, K. Decay Dynamics of Localized Surface Plasmons: Damping of Coherences and Populations of the Oscillatory Plasmon Modes. *Plasmonics* **2019**, *14*, 1629–1637.

(78) Grigorchuk, N. I. Radiative Damping of Surface Plasmon Resonance in Spheroidal Metallic Nanoparticle Embedded in a Dielectric Medium. *J. Opt. Soc. Am. B* **2012**, *29*, 3404.

(79) Melikyan, A.; Minassian, H. On Surface Plasmon Damping in Metallic Nanoparticles. *Appl. Phys. B Lasers Opt.* **2004**, *78*, 453–455.

(80) Hohenester, U. Simulating Electron Energy Loss Spectroscopy with the MNPBEM Toolbox. *Comput. Phys. Commun.* **2014**, *185*, 1177–1187.

(81) Waxenegger, J.; Trügler, A.; Hohenester, U. Plasmonics Simulations with the MNPBEM Toolbox: Consideration of Substrates and Layer Structures. *Comput. Phys. Commun.* **2015**, *193*, 138–150.

(82) Hohenester, U.; Trügler, A. MNPBEM - A Matlab Toolbox for the Simulation of Plasmonic Nanoparticles. *Comput. Phys. Commun.* **2012**, *183*, 370–381.

(83) Novo, C.; Gomez, D.; Perez-Juste, J.; Zhang, Z.; Petrova, H.; Reismann, M.; Mulvaney, P.; Hartland, G. V. Contributions from Radiation Damping and Surface Scattering to the Linewidth of the Longitudinal Plasmon Band of Gold Nanorods: A Single Particle Study. *Phys. Chem. Chem. Phys.* **2006**, *8*, 3540–3546.

(84) Shao, L.; Tao, Y.; Ruan, Q.; Wang, J.; Lin, H.-Q. Comparison of the Plasmonic

Performances Between Lithographically Fabricated and Chemically Grown Gold Nanorods. *Phys. Chem. Chem. Phys.* **2015**, *17*, 10861--10870.

(85) Bosman, M.; Zhang, L.; Duan, H.; Tan, S. F.; Nijhuis, C. A.; Qiu, C. W.; Yang, J. K. W. Encapsulated Annealing: Enhancing the Plasmon Quality Factor in Lithographically-Defined Nanostructures. *Sci. Rep.* **2014**, *4*, 1–6.

(86) Scarabelli, L.; Grzelczak, M.; Liz-Marzán, L. M. Tuning Gold Nanorod Synthesis through Prereduction with Salicylic Acid. *Chem. Mater.* **2013**, *25*, 4232–4238.

(87) Ye, X.; Zheng, C.; Chen, J.; Gao, Y.; Murray, C. B. Using Binary Surfactant Mixtures to Simultaneously Improve the Dimensional Tunability and Monodispersity in the Seeded Growth of Gold Nanorods. *Nano Lett.* **2013**, *13*, 765–771.

(88) Aarle, W. Van; Palenstijn, W. J.; Beenhouwer, J. De; Altantzis, T.; Bals, S.; Batenburg, K. J.; Sijbers, J. The ASTRA Toolbox : A Platform for Advanced Algorithm Development in Electron Tomography. *Ultramicroscopy* **2015**, *157*, 35–47.

(89) Peña, F. de la; Prestat, E.; Fauske, V. T.; Burdet, P.; Jokubauskas, P.; Nord, M.; Ostasevicius, T.; MacArthur, K. E.; Sarahan, M.; Johnstone, D. N.; Taillon, J.; Lähnemann, J.; Migunov, V.; Eljarrat, A.; Caron, J.; Aarholt, T.; Mazzucco, S.; Walls, M.; Slater, T.; Winkler, F.; *et.al.*. *HyperSpy* version1.5.2. *Zenodo* **2019**, doi: 10.5281/zenodo.3396791.

TOC graph

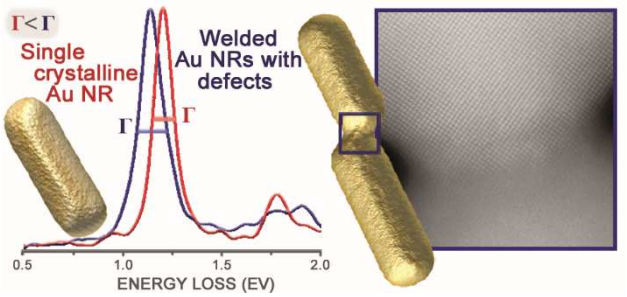
Γ<Γ
Single crystalline Au NR
Welded Au NRs with defects
Γ
Γ
0.5
1.0
1.5
2.0
ENERGY LOSS (EV)